Advanced Engineering Materials

ADVANCED ENGINEERING MATERIALS
www.aem-journal.com

RESEARCH ARTICLE OPEN ACCESS

Near-Field Electrospinning Micro-Printhead Achieves Precise Control of Nanofiber Deposition

Han Xu | Dario Mager | Jan G. Korvink

Institute of Microstructure Technology, Karlsruhe Institute of Technology, Eggenstein-Leopoldshafen, Germany

Correspondence: Dario Mager (dario.mager@kit.edu) | Jan G. Korvink (jan.korvink@kit.edu)

Received: 24 November 2025 | **Revised:** 22 March 2026 | **Accepted:** 17 April 2026

Keywords: additive nanomanufacturing | nanofiber | near-field electrospinning | sub-100-nm fibers

ABSTRACT

As a high-resolution, cost-effective, and rapid fabrication method, near-field electrospinning enables the formation of micro- and nanostructures, positioning it as a promising tool also for advanced nanomanufacturing. However, stable fabrication of sub-100-nm well-aligned fibers remains challenging due to the complex interplay of process parameters. In this work, reliable nanofiber fabrication is established using a custom-built near-field electrospinning setup, based on a micro-printhead having an inner nozzle diameter below 50 µm. A voltage-based classification of jetting region cutoff, fiber formation, and supersaturation is proposed, indicating that continuous nanofiber fabrication is only achievable within a fiber formation parameter region. Thus, augmented by an increase in the relative printhead-substrate velocity, well-placed nanofibers with diameters down to 50 nm are fabricated reproducibly. Additionally, the influence of nozzle outlet size on the required operating voltage and resulting fiber morphology is investigated. This work deepens understanding of the near-field electrospinning process and provides a robust and precise method for fabricating polymer nanofibers as low as 25 nm diameter, contributing a decided advance in facile 3D nanostructuring.

1 | Introduction

Electrospinning, a process within the electrohydrodynamic (EHD) family [1, 2], has attracted significant attention for its ability to produce ultrafine structures, from micro down to nanoscale, with high speed and low cost, making it a promising technique in the field of additive manufacturing. The advantages make it attractive for a wide range of applications, including chemical and biological sensing, tissue engineering, energy storage, and microelectronics [3–5]. Furthermore, by allowing fabrication outside of cleanroom environments, electrospinning reduces cost barriers and facilitates ultrafine fiber production in standard laboratory settings, providing a strong foundation for the development of micro- and nanostructures [6].

In a typical electrospinning process, a liquid droplet (meniscus) is held at the tip of an orifice and subjected to a high electric field. Surface charges accumulate on the droplet, deforming it into a conical shape known as the Taylor cone [7]. When the electric force density exceeds the surface tension pressure, a charged jet is ejected toward a grounded collector, forming fibers significantly thinner than the nozzle diameter [8, 9]. To maintain stable jetting conditions, the liquid—typically a polymer solution—is formulated with low electrical conductivity, to minimize ionic evaporation at the meniscus [10, 11]. Additionally, a continuous pressure or flow rate is applied to ensure a consistent delivery of material [12, 13].

Electrospinning techniques are broadly categorized into far-field electrospinning (FFES) and near-field electrospinning (NFES), based on the working distance between the nozzle and the collector [14, 15]. FFES typically operates at distances greater than 1 cm, where the extended jet path introduces bending instabilities, resulting in randomly oriented nanofibers [16, 17]. In

contrast, NFES uses shorter distances—typically less than 1 cm—which suppresses bending and enables precise, highly aligned deposition [6, 14, 18]. This configuration allows for direct writing of well-defined micro- and submicron structures [2, 19]. The key advantages of NFES include its high deposition resolution, rapid fabrication capability, and compatibility with compact, low-cost systems [3, 20].

Despite the structural simplicity of NFES, controlling fiber diameter and deposition quality at the nanoscale remains challenging due to the complex interplay between electric fields, fluid properties, and environmental conditions [15, 21]. Previous studies have demonstrated that lowering the applied voltage is crucial for reducing fiber diameter. For instance, Chang et al. developed a low-voltage initiation method for NFES [22], and Bisht et al. achieved fiber diameters below 20 nm by fine-tuning voltage parameters [23]. However, in the fabrication of nanofibers using NFES, a comprehensive and systematic investigation of how voltage influences jetting behavior and fiber morphology is still lacking.

In parallel, insights from drop-on-demand EHD jetting (DOD-EHD), which shares similar physical principles with NFES but produces nanodots instead of fibers, have shown that reducing nozzle size to the microscale, or even submicron scale, is critical for achieving nanoscale precision [24–26]. In contrast, NFES systems typically employ nozzles larger than 100 μm in nanoscale fabrication [22, 23, 27]. While DOD-EHD benefits from low-viscosity inks, the higher viscosity of NFES inks poses additional challenges for scaling down nozzle size.

To address these challenges, we reduced the nozzle size to the range of 5–50 μm by employing an anisotropic etching process on a silicon substrate, producing a hollow pyramidal structure with a central through-hole. This Si-based printhead was integrated into a custom-built NFES nanoprinting platform with full control over key process parameters (see Figure 1). Figure 1a shows the overall platform configuration and the integration of the micro-printhead with the collector system, Figure 1b presents representative SEM images of the deposited nanofibers, and Figure 1c illustrates the working principle of jet stretching, solvent evaporation, and nanofiber formation. Using this platform, we successfully fabricated sub-50-nm nanofibers and systematically investigated the influence of two operational factors—applied voltage and substrate motion speed—on jetting behavior and fiber morphology, while keeping the polymer solution unchanged. Additionally, we examined the role of orifice diameter, identifying its critical impact on jet stability, required voltage, and resulting fiber dimensions.

Our findings demonstrate a practical and cost-effective strategy for producing highly uniform sub-50-nm fibers with enhanced jetting stability, enabled by a silicon-based printhead and conducted entirely outside cleanroom conditions. By pushing the resolution limits of precision NFES and clarifying the influence of key parameters, including voltage, substrate speed, and orifice

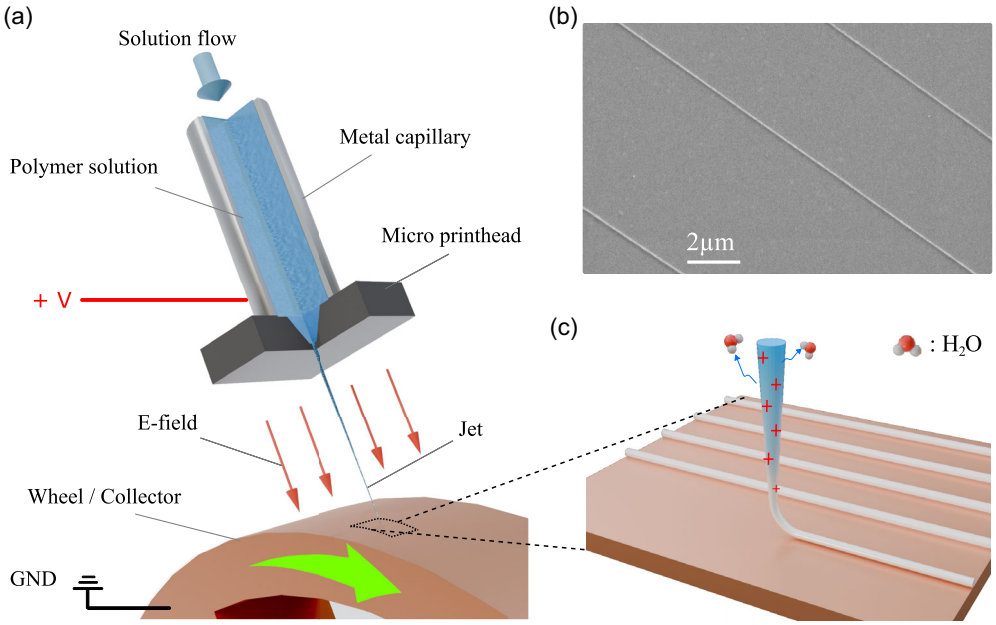

FIGURE 1 | Schematic illustration of the nanofiber deposition process using the Si-based micro-printhead. (a) The micro-printhead is mounted on a metal tip and integrated into a conventional fluid delivery system. The MEMS printhead, produced via anisotropic etching of a silicon substrate, features a hollow pyramidal structure with a flat plateau instead of a sharply tipped bottom. At the center of the plateau, a micro through-hole serves as the outlet for the polymer solution. A polymer jet is emitted under an electric field established between the printhead and a rotating, grounded collector ($r = 75$ mm), positioned at a fixed working distance of 5 mm. The collector moves orthogonally to the rotating plane to align deposited nanofibers in parallel (see the Experimental Section for details). (b) SEM image of the resulting nanofibers deposited on the substrate, with diameters (top right to bottom left) of 40.21, 35.77 and 37.06 nm. (c) Illustration of the printing process using an aqueous polymer solution: The charged jet is elongated and thinned under the electric field, while water evaporates along the jet path, facilitating the formation of solid nanofibers on the substrate.

size, this work advances both the understanding and accessibility of high-precision nanofiber fabrication.

2 | Results and Discussion

2.1 | Three Jetting Regions in NFES

In this work, polyethylene oxide (PEO) was selected as the feedstock polymer due to its widespread use in NFES, its well-established spinnability [28], and suitability for demonstrating the functionality of the MEMS-based NFES printhead. The collector was positioned at a fixed distance of 5 mm from the printhead and rotated at 2 Hz. Printheads featuring a 30 µm orifice were used throughout the study. This configuration was maintained consistently unless otherwise specified.

A critical aspect in the printing process is the flat surface of the printhead where the orifice is located. This design makes it particularly important to prevent wetting effects during jetting (Figure S1a in the Supporting Information). By carefully tuning the flow rate in accordance with the applied voltage, we successfully suppressed wetting (Figure S1b in the Supporting Information) [29–31]. In addition, the variability associated with different printheads of the same nominal size (30 µm) under identical operating conditions was evaluated before the systematic parameter study. The measured orifice sizes and corresponding fiber-diameter distributions showed good consistency across printheads (see Figure S2a,b in the Supporting Information). Therefore, printhead-to-printhead variation was not treated as a separate factor in the following results, and data from printheads of the same nominal size are presented together.

Building upon the printing strategy described above, we examined how key operational parameters influence nanofiber formation using the micro-printhead. The first parameter studied was the applied voltage.

The relationship between applied voltage and fiber diameter is summarized in Figure 2b, which shows a clear trend: The fiber diameter increases significantly with increasing voltage. As noted by Chang et al., nanofibers are observed only at low voltages, while higher voltages result in the deposition of a liquid trace on the substrate [22]. A similar voltage-dependent transition in fiber morphology was also observed in our experiments. In response to this phenomenon, we further propose a classification framework to describe the jetting behavior and deposition morphology in NFES. This framework defines three distinct operational regions—cutoff, fiber formation, and

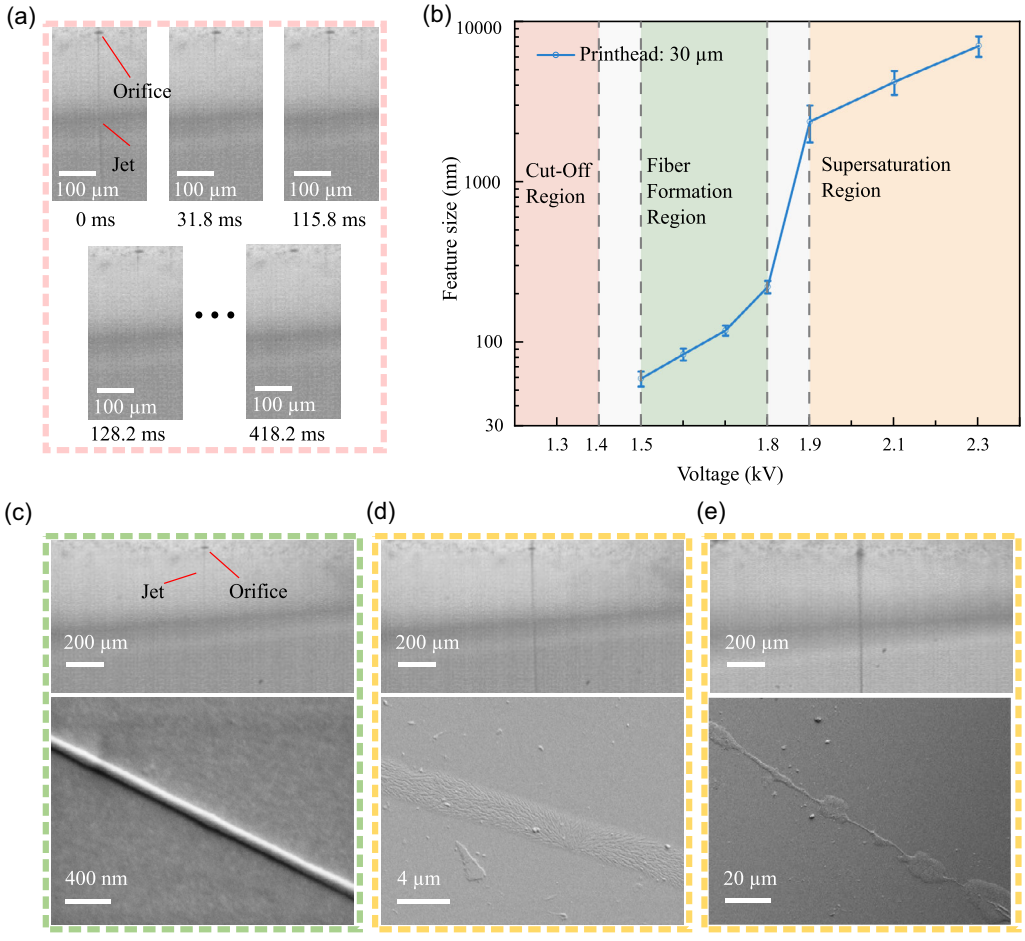

FIGURE 2 | Definition of the three jetting regions. (a) Jetting instability captured by a high-speed camera (5000 fps) during voltage reduction from 1.5 to 1.4 kV. (b) Correlation between applied voltage and the resulting nanofiber morphology. (c–e) Jetting snapshots and corresponding SEM images of depositions at 1.6, 1.9 and 2.5 kV, respectively.

supersaturation—which are color-coded in Figure 2b. These regions are identified based on a combination of jetting images and qualitative observations of deposition from SEM images (Figure 2a,c–e), allowing us to correlate the applied voltage with both jetting stability and deposition outcomes. In the following sections, we analyze each region in detail using both quantitative and visual data.

At low voltages (1.4 kV and below), we define the cutoff region (highlighted in pink in Figure 2b), where no fibers are deposited on the substrate. Due to the chosen voltage increment of 100 V, no data points were collected between 1.4 and 1.5 kV; this range is marked as a transition region (gray zone in Figure 2b). High-speed imaging reveals that the jet becomes unstable and eventually disappears when the voltage drops from 1.5 to 1.4 kV (Figure 2a). The cessation of jetting is not instantaneous: As the voltage decreases from a stable ejection state, the jet undergoes multiple oscillations—alternating between contraction and re-extension—before fully vanishing, taking over 0.4 s to settle. This behavior reflects the delicate balance between electrically induced stress and capillary forces within the liquid. For stable jetting to occur, the electric stress must exceed the opposing capillary force [10, 11]. In the cutoff region, however, capillary forces prevail, resulting in the absence of jetting.

Once the applied voltage reaches 1.5 kV, the electric field becomes strong enough to sustain a continuous jet directed toward the collector. This marks the onset of the fiber formation region (light green in Figure 2b), and 1.5 kV is referred to as its lower limit. In this region, stable jetting is observed in high-speed imaging (Figure 2c, top), and solid, uniform fibers are deposited on the substrate (SEM image in Figure 2c, bottom. Additional low-magnification SEM images illustrating the spatial distribution and alignment of deposited fibers are provided in Figure S5 in the Supporting Information.). The region extends up to 1.8 kV, beyond which significant changes in jetting and deposition are observed and will be discussed below. Within this voltage range, the fiber diameter increases from 59 to 222 nm, as measured from SEM images.

When the applied voltage exceeds 1.8 kV, the jetting process begins to transition toward the supersaturation region. As before, due to the 100 V step size used in the experiments, a second transition zone is defined between 1.8 and 1.9 kV. At 1.9 kV and above, the jet diameter near the orifice increases significantly compared to that in the fiber formation region (Figure 2d, top), and the deposited material forms a wide, continuous trace on the substrate (Figure 2d, bottom). This trace indicates that the jet spreads upon contact with the substrate, forming a liquid-like film rather than solid fibers. Such behavior suggests that solvent evaporation becomes insufficient as the jet radius increases [32, 33], preventing solidification and resulting in broadened, nonfibrous deposition.

As the voltage increases further (2.4 kV and more), the jet diameter continues to grow, and the jetting image (Figure 2e, top) shows an elongated cone with a base diameter matching that of the orifice, further indicating increased jet volume. The corresponding deposition becomes highly irregular and unquantifiable (see SEM image in Figure 2e, bottom); therefore, these data from 2.4 kV are excluded from Figure 2b.

The identification of these three deposition regions contributes to a better understanding of jetting behavior in NFES and is essential for optimizing nanofiber fabrication. Our results show that applied voltage strongly influences both jetting behavior and final fiber morphology. There exists a minimum voltage (here 1.5 kV) required to initiate and maintain jetting, which corresponds to the onset of the fiber formation region. As the voltage increases beyond 1.8 kV, jet diameter grows too large, and solvent evaporation becomes insufficient for fiber solidification, resulting in liquid deposition. In conclusion, high-quality nanofibers can only be fabricated within a low-voltage range (fiber formation region) where the interplay among capillary forces, electric stress, and solvent evaporation is finely tuned.

2.2 | Effect of Substrate Moving Speed on Fiber Morphology

Another critical parameter in the NFES process is the substrate speed [3, 20]. The morphology and features of deposited fibers are expected to vary with different substrate velocities. To investigate this effect, we conducted experiments using the wheel-based collector system described above, where the linear speed of the substrate can be conveniently adjusted by varying the rotation speed of the wheel. For consistency and to aim for the thinnest possible fibers, we selected the lower voltage limit of the fiber formation region (as discussed in Section 2.1) and kept the printhead orifice size constant (30 μm).

Figure 3a shows a clear decreasing trend in fiber diameter as the substrate speed increases from 0.5 to 4 Hz. The plot includes two *x*-axes, representing both rotation frequency and the corresponding linear speed (based on the wheel diameter of 150 mm). At the lowest speed (0.5 Hz), the deposited fibers exhibit a diameter of 91 ± 15 nm and show buckling instability on the substrate (Figure 3d), which can be explained by prior reports [34]. When the rotation speed increases to 1 Hz, the fiber diameter reduces to 65 ± 11 nm, and the buckling instability disappears, resulting in the formation of uniform and well-aligned nanofibers on the substrate (Figure 3e). Further increasing the speed to 2 and 4 Hz leads to additional reductions in fiber diameter, down to 58 ± 7 and 43 ± 7 nm, respectively (Figure 3f,g). At 4 Hz, nanofibers as thin as 25 nm can be observed (see Figure S4 in the Supporting Information) and are included in the diameter distribution shown in Figure 3b. This reduction in diameter is attributed to the enhanced stretching effect exerted by the faster-moving substrate. Remarkably, even at a maximum speed of 4 Hz, the polymer jet remains stable and no fiber breakage is observed on the substrate, highlighting the high stretchability of the polymer solution. To further assess fiber uniformity, we analyzed the diameter of a randomly selected nanofiber at 25 points along a 4-mm segment. The diameter was highly consistent, with a mean of 45.6 nm and a standard deviation of only 3.8 nm (Figure 3c). A Shapiro–Wilk test ($W = 0.98$, $p = 0.96$) confirmed that the measurements follow a Gaussian distribution. Furthermore, the measurement data in Figure 3c, plotted against the measurement index, show a random distribution without a discernible trend. Specifically, linear regression analysis revealed no significant relationship between fiber diameter and measurement index ($p = 0.89$), indicating that the diameters are

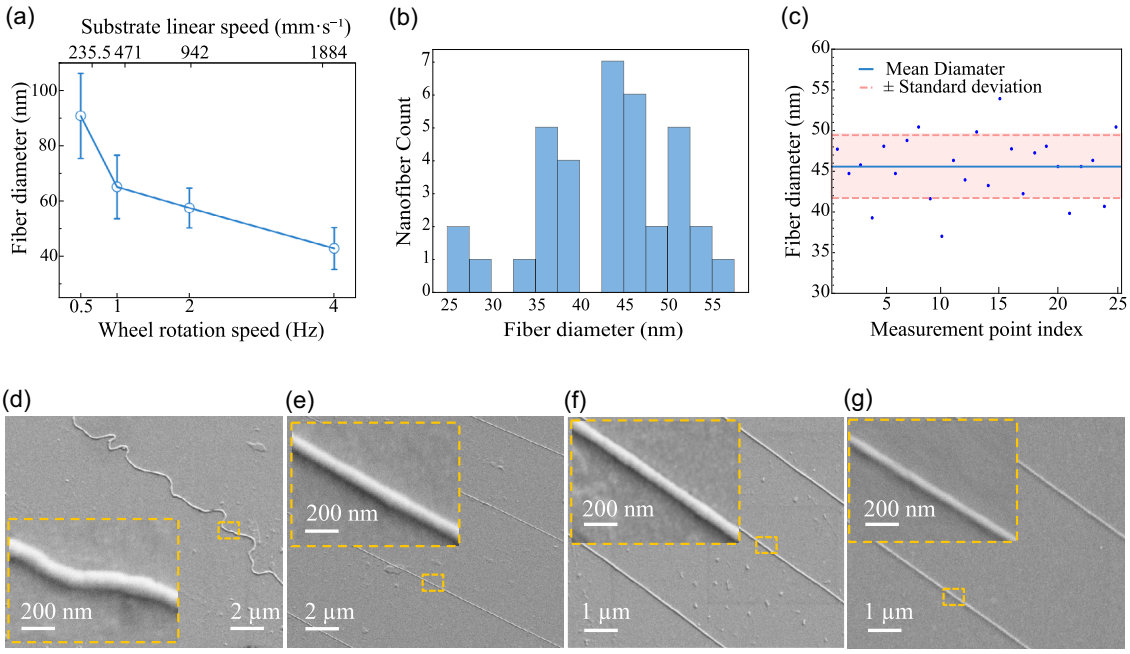

FIGURE 3 | (a) Statistical plot showing the relationship between substrate moving speed and fiber diameter. The *x*-axes represent both rotation frequency (Hz) and the corresponding linear speed (mm/s; wheel diameter, 150 mm). (b) Histogram of the diameter distribution of nanofibers collected at 4 Hz. (c) Diameter distribution measured at 25 points along a single, randomly selected fiber collected at 4 Hz. (d–g) SEM images of fibers collected at rotation frequencies of 0.5, 1, 2 and 4 Hz, respectively, showing both overview and magnified regions to illustrate changes in fiber morphology. (g) The fiber diameter measured directly from the SEM image is approximately 35 nm, highlighting the exceptionally small size achieved.

independent of measurement location and are uniformly distributed along the measured segment.

These results demonstrate that substrate speed significantly influences the morphology of the deposited fibers, particularly in terms of both straightness and diameter. Straight nanofibers are consistently formed only at relatively high substrate speed range, which in this case is above 1 Hz. More importantly, this method offers a simple and cost-effective approach for fabricating ultra-thin nanofibers under conventional experimental environments. By increasing substrate speed, fiber diameters can be easily reduced to sub-50 nm, underscoring the practical advantages of NFES.

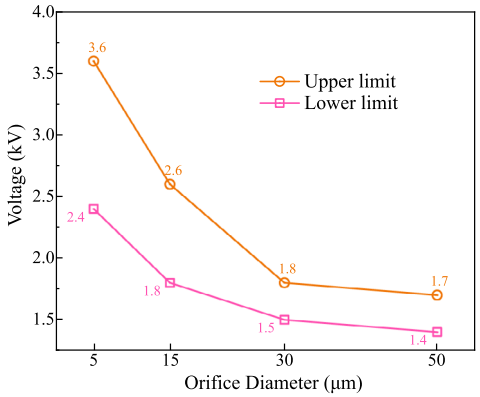

FIGURE 4 | Impact of orifice size on the range of the fiber formation region. The orange line with circular markers represents the upper limit, while the rose line with square markers indicates the lower limit.

2.3 | Effect of Orifice Size on the Voltage Range of the Fiber Formation Region

As discussed in Section 2.1, nanofiber fabrication using the Si-based micro-printhead in NFES requires a low range of applied voltage to remain within the fiber formation region. To investigate the effect of orifice size on this region, we selected four different orifice diameters—50, 30, 15, and 5 μm—manufactured using the same Si-based process.

As shown in Figure 4, the lower limit of the fiber formation region—indicated by rose-colored squares and a connecting line—decreases with increasing orifice size. Specifically, as the orifice diameter increases from 5 to 50 μm, the lower limit drops from 2.4 to 1.4 kV. As previously discussed, this lower limit marks the boundary of the cutoff region, which represents the minimum voltage required to maintain a stable jet in NFES. A smaller orifice leads to a sharper curvature at the liquid–air interface, thereby increasing the capillary pressure. In this context, the capillary effect becomes increasingly significant with decreasing orifice size. As a result, a stronger electric field is required to generate sufficient electric stress to initiate and sustain stable jetting, thereby raising the onset voltage.

Furthermore, the upper limit of the fiber formation region, marked by orange circles and line in Figure 4, also changes with the orifice size. A smaller orifice corresponds to a higher upper limit. Specifically, as the orifice size decreases from 50 to 5 μm, the upper limit increases from 1.7 to 3.6 kV. This trend is partly influenced by the trend of lower limit, where capillary effect plays a role. Moreover, the fiber formation region itself expands with smaller orifices: The voltage range widens from 0.3 to 1.2 kV as the orifice size decreases from 50 to 5 μm. As noted in

Section 2.1, the upper limit defines the boundary between the fiber formation region and the supersaturation region, where liquid traces appear due to insufficient solvent evaporation. For the 50 μm orifice, an increase of just 0.3 kV is sufficient to raise the jet volume enough to surpass the evaporation capacity. In contrast, the 5 μm orifice requires a 1.2 kV increase to reach that threshold. Physically, this boundary is determined by the balance between electric stress driving liquid emission and capillary pressure resisting liquid deformation at the orifice. The electric stress scales approximately as $\tau_e \sim \varepsilon E^2$, while the capillary pressure scales as $P_{cap} \sim 2\gamma/r$. Because smaller orifices correspond to a smaller radius r, the capillary pressure is larger and therefore more strongly counteracts the increase in electric stress, leading to a more gradual increase in jet thickness with voltage. As a result, the jet can remain fully solidified over a wider voltage range before wet deposition occurs. Consequently, smaller orifices exhibit a broader operational window.

In summary, the orifice size of the Si-based micro-printhead significantly influences the operating voltage range of the fiber formation region. Primarily, surface tension associated with different orifice sizes affects both the lower and upper voltage limits of this range. Moreover, the orifice size substantially impacts the width of the operational window. This effect arises from the interplay between surface tension and the sensitivity of jet volume to voltage variations across orifice sizes.

2.4 | Effect of Orifice Size on Fiber Morphology

To further investigate the effect of orifice size on fiber morphology in NFES using the micro-printhead, the same ones used in Section 2.3 are used here. Since our focus is on nanofiber fabrication, only the fiber formation region is considered in this analysis. To eliminate the influence of varying thresholds of the fiber formation region for different orifice sizes, the operational voltage limits established in Section 2.3 are used. A dimensionless voltage parameter, α, is introduced and defined as the normalized difference between the applied voltage and the lower limit of the fiber formation region and has a range from 0 to 1:

$$\alpha = \frac{V_{applied} - V_{min}}{V_{max} - V_{min}}$$

Figure 5a shows the relationship between the dimensionless voltage and fiber diameter on a logarithmic scale ($\log_{10}$) for improved visualization. The data for the 30 μm printhead, already discussed in Section 2.1, are included here for data integrity. A clear positive correlation between applied voltage and fiber diameter is observed across all orifice sizes, consistent with the trends described in Section 2.1.

At the lower voltage limit ($\alpha = 0$), all printheads are capable of producing sub-100-nm fibers. Moreover, a positive correlation is observed between fiber diameter and orifice size at $\alpha = 0$. Specifically, the 5 μm printhead produces fibers with diameters as low as 53 ± 8 nm (Figure 5b left), while the 50 μm printhead yields fibers with diameters of 78 ± 9 nm (Figure 5c left). Despite the large difference in orifice size, the corresponding fiber diameters differ only modestly, indicating that simply reducing nozzle size does not dramatically affect the minimum achievable fiber diameter.

The most significant differences among printheads appear at the upper limit of the fiber formation region ($\alpha = 1$). Unlike at the lower limit, fiber diameter at the upper limit increases markedly with decreasing orifice size. The thickest fibers, measuring 832 ± 95 nm, are produced using the 5 μm printhead (Figure 5b right), whereas the 50 μm printhead produces a maximum fiber diameter of only 102 ± 10 nm (Figure 5c right). This behavior is consistent with the broader operational window discussed above, which allows thicker fibers to form before the transition to wet deposition occurs. The 15 and 30 μm printheads follow the same trend. In addition, the four curves in Figure 5a exhibit different growth rates of fiber diameter with increasing dimensionless voltage, reflecting the range of fiber diameters achievable with each printhead. The 5 μm printhead achieves a fiber-diameter range ratio of 15.8 (thickest/thinnest), compared to only 1.3 for the 50 μm printhead. This difference of ratios indicates that the printheads with smaller orifice provide a broader range of fiber diameters, which is beneficial for applications requiring tunability.

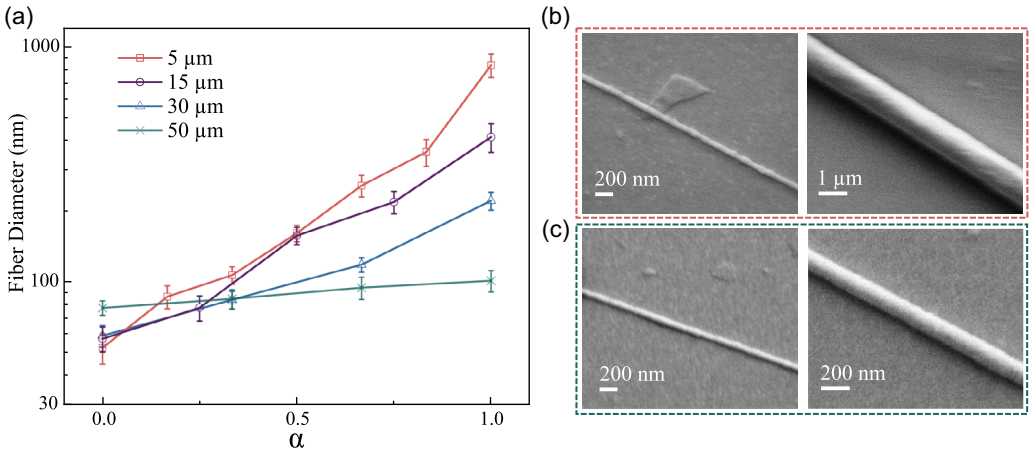

FIGURE 5 | Impact of orifice size on fiber morphology. (a) Statistical data showing the relationship between normalized voltage and fiber diameter for four orifice sizes. (b) Representative SEM images of fibers fabricated with a 5 μm printhead at $\alpha = 0$ and $\alpha = 1$, respectively, corresponding to the extremities of the red line in (a). (c) Representative SEM images of fibers fabricated with a 50 μm printhead at $\alpha = 0$ and $\alpha = 1$, respectively.

In summary, smaller orifices—such as the 5 μm one—offer certain advantages in NFES, including the ability to produce sub-50-nm fibers and a broader range of tunable fiber diameters. However, the improvement in minimum achievable diameter is relatively modest compared to the significant reduction in orifice size, indicating that orifice miniaturization alone is not an effective strategy for dramatically reducing fiber diameter. Moreover, smaller orifices are more prone to clogging, making them more difficult to operate under consistent conditions compared to larger orifices such as 30 and 50 μm. This necessitates stricter requirements for solution cleanliness, stability, and storage. This operational constraint should be carefully considered when selecting the appropriate printhead orifice size for a given application. From a practical perspective, the choice of orifice size therefore depends on the balance between tunability and operational robustness. Smaller orifices provide the widest accessible fiber-diameter range, but require stricter control of solution preparation, printhead cleanliness, handling and storage conditions, and startup operation because of their higher susceptibility to clogging. Larger orifices, although offering a narrower tunable diameter window, provide more robust and repeatable operation and may therefore be more practical for stable long-term processing.

3 | Conclusion

This work focused on nanofiber fabrication using NFES, emphasizing the investigation of key process parameters on jetting behavior and fiber morphology. Leveraging a custom-built system, we achieved precise control over critical parameters including voltage and collection speed. Instead of conventional needles, Si-based micro-printheads with diameters varying from 5 to 50 μm were employed, enabling a detailed examination of orifice size effects on nanofiber formation.

Specifically, we defined three voltage-dependent regions—cutoff, fiber formation, and supersaturation—classified according to the observed jetting behavior and deposition morphology, and parameterized by the applied electrospinning voltage. Our results show that uniform and solid nanofibers can be reliably produced only within the fiber formation region and that reducing the applied voltage within this region decreases fiber diameter. Additionally, the substrate translation speed was found to further influence fiber morphology. By combining a low voltage (the lower limit of the fiber formation region) with a high substrate speed of $v = 2\pi r \times f = 2\pi \times 0.075 \times 4 = 1.88\,\mathrm{ms}^{-1}$, we achieved nanofibers below 50 nm in diameter, including fibers as thin as 25 nm.

We also explored how orifice size affects the boundaries of the fiber formation region and the resulting fiber morphology. While smaller orifices enable finer control and broader tunability in fiber dimensions, they also introduce challenges such as increased clogging and stricter requirements for solution and equipment cleanliness. These trade-offs must be considered when selecting printhead sizes for specific applications.

Although the present study focused on an aqueous PEO system as a model material, the underlying NFES mechanism and the printhead-based deposition strategy are not restricted to PEO alone. For other electrospinnable material systems, stable jet formation would require appropriate adjustment of solution properties, such as concentration, viscosity, conductivity, and solvent composition, together with corresponding optimization of the operating conditions.

Overall, this study demonstrates not only the feasibility but also the precise controllability of nanofiber fabrication using NFES. The printing approach is low cost and does not require cleanroom facilities, making it a highly promising method for controllable and accessible nanofiber manufacturing.

4 | Experimental Section

4.1 | Fabrication of Si-Based Micro-Printhead

Figure 6 shows the standard Si-MEMS manufacturing process used to produce the electrospinning printheads and labels the processing steps. (1) A 100-mm ⟨1, 0, 0⟩ silicon wafer was sputter-coated with 400 nm SiN on both faces. (2) On the back side of the wafer, a square window of 1 mm side length was opened in the SiN to expose the silicon wafer surface and define the base of a pyramidal recess. (3) The Si wafer was anisotropically etched through the SiN window, using KOH. The etch was stopped before penetrating the top surface of the wafer, leaving a thin Si and SiN layer. (4) A second lithography step, on the front of the wafer, defined the 30-μm-diameter through-hole into the tip of the pyramid. (5) Both the Si and SiN layers were reactive ion etched through the opening. (6) The SiN was removed from the backside of the wafer using reactive ion etching, after which the backside of the wafer was sputter-coated with a thin Cr and Au layer, to form the biasing electrode of the printhead.

4.2 | Experimental Setup

A detailed schematic of the experimental setup is shown in Figure 7a. A high-speed camera (Phantom V210) equipped with a macro lens (25 mm, f/2.8, 2.5–5.0 ×)was mounted on an

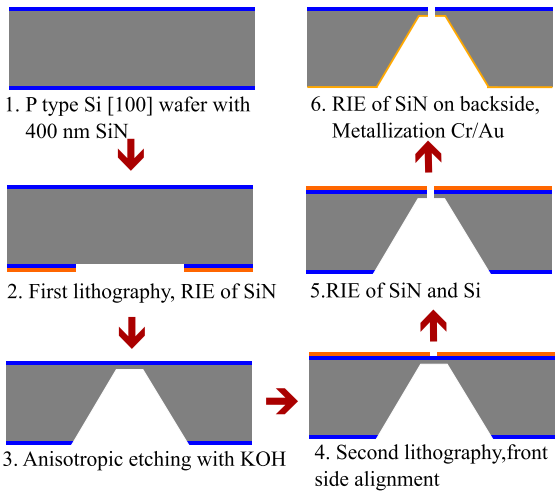

FIGURE 6 | Si-MEMS micro-printhead manufacturing process.

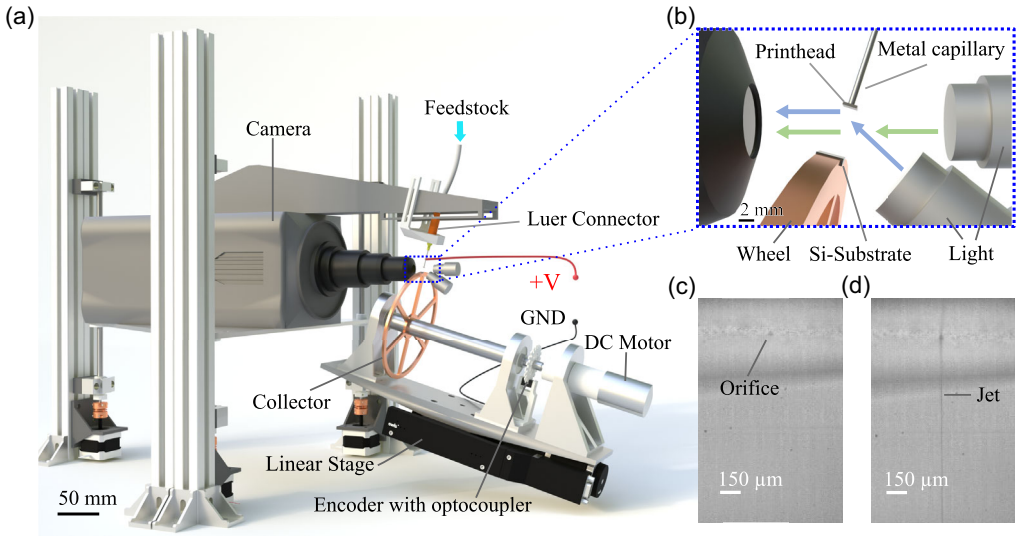

FIGURE 7 | The self-built NFES setup. (a) 3D CAD model of the setup showing the geometrical arrangement. (b) Zoomed-in diagram of the imaging system. The camera objective is on the left, with the primary and secondary light sources on the right. Light blue arrows indicate light emitted from the obliquely positioned primary source, reflected by the printhead surface, and captured by the camera objective. Green arrows indicate the silhouette path, where light from the secondary source travels through the jet toward the camera. (c,d) Representative high-speed camera images of the printhead without and with jetting.

adjustable vertical frame for flexible imaging. The alignment between the printhead and camera was stabilized using a rigid truss to maintain consistent visualization during operation.

The printhead was connected to a Luer tip, which was linked via PTFE tubing to a 1-mL syringe mounted on a syringe pump (Chemxy F100) to deliver a stable flow rate. Before use, the solution was filtered through a 1-µm syringe filter to remove particulates and reduce the risk of clogging. A rotating collector, driven by a DC motor, provided unidirectional motion. A gear-shaped encoder with optocoupler was mounted on the collector axis to measure rotation speed. A linear stage (Owis LTM80) enabled translational movement orthogonal to the rotation plane. A high-voltage power supply (Heinzinger PNChp 6000) applied the electric field, with the printhead held at high voltage and the collector grounded. A 3×4 mm p-doped silicon chip (1 to 10 Ω cm, thickness, 525 ± 25 nm), mounted on the collector, was used as the substrate for nanofiber deposition. The combination of the silicon substrate and the metallic collector components facilitated dissipation of residual charge through the ground connection [35, 36].

To capture both the printhead surface and the electrospun jet, the imaging system was configured using an angled illumination strategy. As shown in Figure 7b, the primary light source and the camera were positioned at a 30° angle relative to each other, while the printhead was tilted at 15° to reflect surface features into the lens. The reflection from the printhead surface is illustrated in Figure 7c. The collector was correspondingly inclined to maintain proper alignment. In addition, a secondary fiber-optic light source, aligned with the camera's optical axis, was employed to produce a silhouette of the jet. This dual-path imaging setup allowed simultaneous visualization of the jet, which appeared as a combined silhouette—one from reflection off the printhead surface, and the other from direct backlighting by the secondary light source (Figure 7d).

4.3 | Solution Preparation

Polyethylene oxide (PEO, M.W.: 300 K; Alfa Aesar) was used as the polymer feedstock. The solvent was deionized water. A 5 wt% PEO solution was prepared by stirring the polymer in water at 500 rpm for 12 h at room temperature. The aqueous PEO solution exhibited clear shear-thinning behavior over the measured shear-rate range. The apparent viscosity decreased from 562 mPa · s at 50 s^{-1} to 88.2 mPa · s at 9000 s^{-1} (23°C), measured using a rotational rheometer [37] [38]. The full viscosity curve is provided in Figure S6 in the Supporting Information.

4.4 | NFES Process

To initiate jetting under low-voltage, low-flow rate conditions, a mechanical triggering method known as "poking" was used here [22]. In NFES, the electric field required to initiate jet formation is typically higher than that required to sustain stable jetting; therefore, a small mechanical perturbation is often used to trigger the jet directly at the stable operating voltage. A thin wooden stick was gently brought into contact with the orifice and then withdrawn, pulling out a fine filament. This residual filament, together with the perturbed liquid interface, serves as a seed for stable jet formation under the applied electric field (see Figure S3 in the Supporting Information). The reproducibility of this mechanical triggering method was evaluated in multiple startup experiments, and the corresponding success rates are summarized in Table S1 in the Supporting Information.

To reduce the risk of clogging, the capillary and printhead were cleaned by blowing with air before use. In addition, the triggering procedure was carried out as quickly as possible after liquid appeared at the orifice, thereby minimizing stagnation at the tip. When partial clogging occurred, flow recovery could in some cases be achieved for 30 to 50 µm orifices by applying a brief

flushing pressure within the first few minutes after loading. For smaller orifices, however, this recovery approach was less effective.

Stable jetting is defined as being able to maintain a jet under operating conditions for 1 min without break-up.

All experiments were conducted under ambient laboratory conditions at approximately 20°C to 25°C and 35%–50% relative humidity.

4.5 | Characterization

The MEMS printheads were inspected by optical microscopy (Keyence VHX-100) before use to determine the orifice size and to check for obvious defects or dust contamination.

The morphology of the electrospun nanofibers was characterized using a scanning electron microscope (Carl Zeiss SUPRA 60VP SEM). Samples were sputter-coated with a 10 nm Au/Pd layer (EMITECH K575X, 30 mA, 120 s) to reduce surface charging. Fiber diameters were measured directly using the SEM's built-in measurement tool.

Acknowledgments

The authors hereby acknowledge financial support from the Deutsche Forschungsgemeinschaft (DFG, German Research Foundation) under Germany's Excellence Strategy via the Excellence Cluster 3D Matter Made to Order (EXC-2082/1–390761711). The authors acknowledge the support of the Helmholtz Society through the program Materials Systems Engineering, Research Area Information, and appreciate the support of Dr. Bharat Sharma and the IMT cleanroom team for manufacturing the silicon printhead.

Open Access funding enabled and organized by Projekt DEAL.

Funding

This study was supported by Deutsche Forschungsgemeinschaft (Grant EXC-2082/1–390761711) and Helmholtz-Gemeinschaft (43.35.02).

Conflicts of Interest

The authors declare no conflicts of interest.

Data Availability Statement

The data that support the findings of this study are available from the corresponding author upon reasonable request.

References

1. A. Reizabal, B. Tandon, S. Lanceros-Méndez, and P. D. Dalton, "Electrohydrodynamic 3d Printing of Aqueous Solutions," *Small* 19, no. 7 (2023): 2205255.

2. Y. A. Huang, N. Bu, Y. Duan, et al., "Electrohydrodynamic Direct-Writing," *Nanoscale* 5, no. 24 (2013): 12007–12017.

3. Y. Huang, Y. Li, Y. Zhang, H. Yu, and Z. Tan, "Near-Field Electrospinning for 2d and 3d Structuring: Fundamentals, Methods, and Applications," *Materials Today Advances* 21 (2024): 100461.

4. Y. Li, J. Zhu, H. Cheng, et al., "Developments of Advanced Electrospinning Techniques: A Critical Review," *Advanced Materials Technologies* 6, no. 11 (2021): 2100410.

5. A. Randhawa, S. D. Dutta, K. Ganguly, T. V. Patil, and K.-T. Lim, "Manufacturing 3d Biomimetic Tissue: A Strategy Involving the Integration of Electrospun Nanofibers with a 3d-Printed Framework for Enhanced Tissue Regeneration," *Small* 20, no. 27 (2024): 2309269.

6. D. Ji, Y. Lin, X. Guo, et al., "Electrospinning of Nanofibres," *Nature Reviews Methods Primers* 4, no. 1 (2024): 1.

7. G. I. Taylor, "Electrically Driven Jets," *Proceedings of the Royal Society of London. A. Mathematical and Physical Sciences* 313, no. 1515 (1969): 453–475.

8. I. Marginean, L. Parvin, L. Heffernan, and A. Vertes, "Flexing the Electrified Meniscus: The Birth of a Jet in Electrosprays," *Analytical Chemistry* 76, no. 14 (2004): 4202–4207.

9. J. J. Feng, "The Stretching of an Electrified Non-Newtonian Jet: A Model for Electrospinning," *Physics of Fluids* 14, no. 11 (2002): 3912–3926.

10. J. F. de La Mora, "The Fluid Dynamics of Taylor Cones," *Annual Review of Fluid Mechanics* 39, no. 1 (2007): 217–243.

11. D. A. Saville, "Electrohydrodynamics: The Taylor-Melcher Leaky Dielectric Model," *Annual Review of Fluid Mechanics* 29, no. 1 (1997): 27–64.

12. J. F. De La Mora and I. G. Loscertales, "The Current Emitted by Highly Conducting Taylor Cones," *Journal of Fluid Mechanics* 260 (1994): 155–184.

13. A. M. Gañán-Calvo, J. Davila, and A. Barrero, "Current and Droplet Size in the Electrospraying of Liquids. Scaling Laws," *Journal of Aerosol Science* 28, no. 2 (1997): 249–275.

14. D. Sun, C. Chang, S. Li, and L. Lin, "Near-Field Electrospinning," *Nano Letters* 6, no. 4 (2006): 839–842.

15. M. M. Nazemi, "Alireza Khodabandeh, and Afra Hadjizadeh. Near-Field Electrospinning: Crucial Parameters, Challenges, and Applications," *ACS Applied Bio Materials* 5, no. 2 (2022): 394–412.

16. D. H. Reneker, A. L. Yarin, H. Fong, and S. Koombhongse, "Bending Instability of Electrically Charged Liquid Jets of Polymer Solutions in Electrospinning," *Journal of Applied Physics* 87, no. 9 (2000): 4531–4547.

17. D. H. Reneker and A. L. Yarin, "Electrospinning Jets and Polymer Nanofibers," *Polymer* 49, no. 10 (2008): 2387–2425.

18. X.-X. He, J. Zheng, G.-F. Yu, et al., "Near-Field Electrospinning: Progress and Applications," *The Journal of Physical Chemistry C* 121, no. 16 (2017): 8663–8678.

19. M. Lee and H.-Y. Kim, "Toward Nanoscale Three-Dimensional Printing: Nanowalls Built of Electrospun Nanofibers," *Langmuir* 30, no. 5 (2014): 1210–1214.

20. G. Zheng, W. Li, X. Wang, D. Wu, D. Sun, and L. Lin, "Precision Deposition of a Nanofibre by Near-Field Electrospinning," *Journal of Physics D: Applied Physics* 43, no. 41 (2010): 415501.

21. S. A. Theron, E. Zussman, and A. L. Yarin, "Experimental Investigation of the Governing Parameters in the Electrospinning of Polymer Solutions," *Polymer* 45, no. 6 (2004): 2017–2030.

22. C. Chang, K. Limkrailassiri, and L. Lin, "Continuous Near-Field Electrospinning for Large Area Deposition of Orderly Nanofiber Patterns," *Applied Physics Letters* 93, no. 12 (2008): 123111.

23. G. S. Bisht, G. Canton, A. Mirsepassi, et al., "Controlled Continuous Patterning of Polymeric Nanofibers on Three-Dimensional Substrates Using Low-Voltage Near-Field Electrospinning," *Nano Letters* 11, no. 4 (2011): 1831–1837.

24. J.-U. Park, M. Hardy, S. J. Kang, et al., "High-Resolution Electrohydrodynamic Jet Printing," *Nature Materials* 6, no. 10 (2007): 782–789.

25. J. Schneider, P. Rohner, D. Thureja, M. Schmid, P. Galliker, and D. Poulikakos, "Electrohydrodynamic Nanodrip Printing of High Aspect Ratio Metal Grid Transparent Electrodes," *Advanced Functional Materials* 26, no. 6 (2016): 833–840.

26. P. Galliker, J. Schneider, H. Eghlidi, and S. Kress, "Vahid Sandoghdar, and Dimos Poulikakos. Direct Printing of Nanostructures by Electrostatic Autofocussing of Ink Nanodroplets," *Nature Communications* 3, no. 1 (2012): 890.

27. N. Mkhize and H. Bhaskaran, "Electrohydrodynamic Jet Printing: Introductory Concepts and Considerations," *Small Science* 2, no. 2 (2022): 2100073.

28. W. E. King III and G. L. Bowlin, "Near-Field Electrospinning and Melt Electrowriting of Biomedical Polymers—progress and Limitations," *Polymers* 13, no. 7 (2021): 1097.

29. B. He, S. Yang, Z. Qin, B. Wen, and C. Zhang, "The Roles of Wettability and Surface Tension in Droplet Formation during Inkjet Printing," *Scientific Reports* 7, no. 1 (2017): 11841.

30. A. Lee, H. Jin, H.-W. Dang, K.-H. Choi, and K. H. Ahn, "Optimization of Experimental Parameters to Determine the Jetting Regimes in Electrohydrodynamic Printing," *Langmuir* 29, no. 44 (2013): 13630–13639.

31. M. Yu, K. H. Ahn, and S. J. Lee, "Design Optimization of Ink in Electrohydrodynamic Jet Printing: Effect of Viscoelasticity on the Formation of Taylor Cone Jet," *Materials & Design* 89 (2016): 109–115.

32. G. Collins, J. Federici, Y. Imura, and L. H. Catalani, "Charge Generation, Charge Transport, and Residual Charge in the Electrospinning of Polymers: A Review of Issues and Complications," *Journal of Applied Physics* 111, no. 4 (2012): 044701.

33. X.-F. Wu, Y. Salkovskiy, and Y. A. Dzenis, "Modeling of Solvent Evaporation from Polymer Jets in Electrospinning," *Applied Physics Letters* 98, no. 22 (2011): 223108.

34. T. Han, D. H. Reneker, and A. L. Yarin, "Buckling of Jets in Electrospinning," *Polymer* 48, no. 20 (2007): 6064–6076.

35. I. Liashenko, J. Rosell-Llompart, and A. Cabot, "Ultrafast 3d Printing with Submicrometer Features Using Electrostatic Jet Deflection," *Nature Communications* 11, no. 1 (2020): 753.

36. A. Sadaf, M. Elter, D. Mager, U. H. F. Bunz, M. Islam, and J. G. Korvink, "Wall Microstructures of High Aspect Ratio Enabled by Near-Field Electrospinning," *Advanced Engineering Materials* 24, no. 9 (2022): 2101740.

37. A. L. Yarin, F. Pierini, E. Zussman, L. Marco, et al., *Materials and Electro-Mechanical and Biomedical Devices Based on Nanofibers* (Springer, 2024).

38. K. W. Ebagninin, A. Benchabane, and K. Bekkour, "Rheological Characterization of Poly (ethylene Oxide) Solutions of Different Molecular Weights," *Journal of Colloid and Interface Science* 336, no. 1 (2009): 360–367.

Supporting Information

Additional supporting information can be found online in the Supporting Information section.